Advancing the Coupling of III-V Quantum Dots to Photonic Structures to Shape Their Emission Diagram

Erwan Bossavit, Oleksandra Yeromina, Dario Mastrippolito, Mariarosa Cavallo, Huichen Zhang, Tommaso Gemo, Albin Colle, Adrien Khalili, Andrei Shcherbakov, Lam Do Nguyen, et al.

▶ To cite this version:

Erwan Bossavit, Oleksandra Yeromina, Dario Mastrippolito, Mariarosa Cavallo, Huichen Zhang, et al.. Advancing the Coupling of III-V Quantum Dots to Photonic Structures to Shape Their Emission Diagram. Advanced Optical Materials, 2024, pp.2401601. 10.1002/adom.202401601 . hal-04715223

HAL Id: hal-04715223

https://hal.science/hal-04715223v1

Submitted on 30 Sep 2024

Advancing the Coupling of III–V Quantum Dots to Photonic Structures to Shape Their Emission Diagram

*Erwan Bossavit, Oleksandra Yeromina, Dario Mastrippolito, Mariarosa Cavallo, Huichen Zhang, Tommaso Gemo, Albin Colle, Adrien Khalili, Andrei Shcherbakov, Lam Do Nguyen, Claire Abadie, Erwan Dandeu, Mathieu G. Silly, Bruno Gallas, Debora Pierucci, Aloyse Degiron, Peter Reiss, and Emmanuel Lhuillier**

The development of optoelectronic devices based on III–V semiconductor colloidal quantum dots (CQDs) is highly sought after due to their reduced toxicity. While devices based on conventional CQDs (II–VI semiconductors, halide perovskites) have achieved impressive technological leaps since their discovery, the most mature of these compounds contain toxic heavy metal elements (Cd, Hg, or Pb), which are highly undesirable for safe industrial scale applications. The strong covalent bonds of III–V compounds like InP, InAs, or InSb prevent the release of their toxic atoms, making them safer. However, these same bonds create severe material constraints. Namely, their harsher reaction conditions and increased sensitivity to oxidation have kept most of the research focused on material development. Meanwhile, their integration into devices and their coupling to photonic structures lag behind. Here, the integration of InAs/ZnSe core-shell CQDs is advanced. First, the material parameters necessary to design plasmonic gratings coupled to the CQDs are elucidated and those gratings are fabricated. Angle-resolved spectroscopy shows that the plasmon modes successfully couple to the CQD layer's emission leading to a tunable directivity with a 15° linewidth. A 3-fold increase of the PL signal is achieved at normal incidence, thus advancing toward the goal of efficient outcoupling in LEDs.

1. Introduction

The success of colloidal quantum dots (CQDs) is strongly connected to their ability to be obtained through the large-scale synthesis of nanomaterials presenting an atom-like spectrum. Among the main advances in the development of colloidal syntheses, one can cite the achievement of a roughness-free synthesis[1] (i.e., without size dispersion) where the width of the photoluminescence (PL) spectrum is only limited by the homogeneous broadening, as well as the successful growth of complex colloidal heterostructures.[2–4] Despite this progress, to date, colloidal syntheses work best for compounds with strong ionic bonds like II-VI semiconductors and halide perovskites. The reduced formation energy of ionic bonds compared to covalent bonds makes them easier to be formed under mild conditions, i.e., temperatures compatible with solution synthesis. However, most of the

---

E. Bossavit, D. Mastrippolito, M. Cavallo, H. Zhang, T. Gemo, A. Colle, A. Khalili, A. Shcherbakov, L. D. Nguyen, C. Abadie, E. Dandeu, B. Gallas, D. Pierucci, E. Lhuillier
Institut des NanoSciences de Paris
Sorbonne Université, CNRS
Paris 75005, France
E-mail: el@insp.upmc.fr

E. Bossavit, M. G. Silly
Synchrotron SOLEIL, L'Orme des Merisiers
Départementale 128, Saint-Aubin 91190, France

O. Yeromina, P. Reiss
Univ. Grenoble Alpes, CEA, CNRS, IRIG, SyMMES
Grenoble 38000, France

A. Degiron
Laboratoire Matériaux et Phénomènes Quantiques
Université Paris Cité, CNRS
Paris 75013, France

The ORCID identification number(s) for the author(s) of this article can be found under https://doi.org/10.1002/adom.202401601

DOI: 10.1002/adom.202401601

strongly ionic compounds of interest for CQDs include at least one heavy metal element (Cd, Pb, or Hg), whose presence is often seen as a bottleneck for the transfer of those CQDs toward industrial applications.

To address this question, a large effort has been devoted to the growth of III–V compounds made of InP,[5,6] InAs,[7,8] or InSb.[9–11] Their strong covalent bonds make them less likely to release toxic atoms, making them less dangerous from a safer-by-design perspective. This same aspect however also makes them less suitable for colloidal synthetic routes. Therefore, novel synthetic schemes have been proposed recently, either through the use of more reactive, and even possibly pyrophoric precursors, the use of strong reducing agents,[12] the development of new synthetic procedures,[12–14] or the use of molten salts[15] to raise the reaction temperature (up to 350 °C). Beyond these challenges, the III–V CQDs also show an increased tendency for oxidation, pushing the need for the development of core-shell heterostructures. However, on top of the usual considerations of good band alignment and reduced lattice mismatch, the constraint of being heavy metal-free further limits the choice of materials for the shell, reducing the selection to Zn-based materials. Together, these synthetic challenges have kept the research relative to III–V CQDs (except for InP) mostly focused on material considerations (i.e., new synthetic schemes,[16] doping,[17–19] pushing the spectral range by growing a broader range of sizes,[20] or achieving core-shell[21–23] materials), while device[23–28] integration and photonic coupling lag clearly behind.

This situation contrasts with the case of other narrow bandgap CQDs such as PbS[29] and HgTe,[30] whose high maturity now ensures their use as infrared photoactive solution-processable inks. Hence, the focus for research is no longer driven by material considerations but rather by advanced applications. Recent results[23,31–33] have nevertheless pushed the growth of III–V CQDs toward narrower bandgaps, while shell growth[7,34] has greatly enhanced the stability of the material, making the exploration of their optoelectronic performances worthwhile. When it comes to infrared devices based on III–V CQDs, most of the reported works are dedicated to vertical photodiode stacks either for light emission[33] or photodetection.[23–25,27,28] The spotlight is currently given to the electrical aspects, but such devices also suffer from incomplete light-matter coupling. The absorption in these stacks remains far from unity, while the emission from light-emitting diodes is poorly coupled to the far field, requiring more directive emission.

Here, we explore the integration of InAs/ZnSe core-shell CQDs into a photonic structure as a strategy to achieve a directive emission. We use the optical properties of the material as an input to design a metallic grating supporting surface-plasmon polaritons (SPPs) while covered by a film of CQDs. We then demonstrate that the emission from the CQDs couples to the SPP, which allows the directivity of the emission to be tuned.

2. Results and Discussion

We start by growing and characterizing InAs/ZnSe core-shell[35] CQDs on the basis of previously optimized reported procedures.[14,32] The projection of the tetrahedral CQDs using transmission electron microscopy leads to triangular shapes with an edge length of 10.2 ± 1.8 nm, see **Figure 1a**. This size is chosen[36] to obtain an optical feature in the near-infrared with a maximum of absorption at ≈900 nm (Figure 1b), and a well-defined PL peak centered at 1020 nm. The presence of a shell ensures that the PL is stable (Figure S1, Supporting Information) enough to allow for later characterization in air, which is not the case for films of core-only InAs. To obtain a film, the material is spin-coated so that no ordering of the CQDs is expected.

X-ray photoemission spectroscopy is used to confirm the presence of the shell and quantify the oxidation of the material, see Figure 1c, and Figures S2 and S3 (Supporting Information). The survey spectrum confirms the presence of In, As, Zn, and Se. In addition, we notice the presence of S, which results from the ligand exchange performed on the film (solid-state ligand exchange carried out by dipping the film in a solution of Na_2S in ethanol) to increase its conductivity and therefore prevent sample charging. The ligand exchange is not conducted for the films dedicated to PL characterization in order to maintain a higher PL efficiency and ensure a better signal. Carbon is associated with a leftover of the long-chained native ligands (oleylamine) used during the growth. The presence of oxygen is also detected, with nevertheless a limited amplitude. More information relative to possible oxidation can be obtained by analyzing the core levels, see Figures S2 and S3 (Supporting Information). The core levels relative to the shell material, Zn 3d and Se 3d display single contributions with binding energies at 10.3 and 54.5 eV respectively, see Figure S2 (Supporting Information). Concerning the core levels relative to the core material, the In 3d signal mostly displays a single contribution with a main peak at 445 eV. This value is close to what has been reported for In bounded to Sb in InSb CQD when probed with soft X-rays.[37] A second, much weaker contribution at 445.8 eV can be attributed to indium oxide. The only core level that displays evidence for oxidation is As 3d. The comparison with the core-only material (Figure S3, Supporting Information) shows that the relative weight of the oxide is strongly reduced once the material is shelled. Summarizing, these analyses confirm that InAs/ZnSe CQDs display optical features in the infrared, while also being stable enough to envision further coupling to a photonic structure.

To complete the preliminary studies, we prepared a thin film of pristine InAs/ZnSe CQDs and measured its complex optical index through spectrally resolved ellipsometry. The refractive index (n) is found to be weakly spectrally dependent with a typical value of ≈1.9, i.e., much weaker than $\sqrt{\varepsilon_r}$, with $\varepsilon_r = 15$ the dielectric constant of bulk InAs.[38] This discrepancy reflects the presence of empty spaces and/or organic molecules in the CQD film, which is expected as no ligand exchange was carried out here. The extinction coefficient (k) spectrum follows closely the absorption spectrum, while the value of k at the band edge is determined to be 0.06.

In a second step, we prepared a series of plasmonic gratings to give directivity to the emission of the CQDs. This approach has been proven as a viable strategy to shape and tune the luminescence of a broad variety of CQDs including 2D nanoplatelets,[39–41] perovskites,[42] PbS,[43] or HgTe.[44,45] Here, we specifically designed the grating on the top of a gold mirror, see **Figures 2a** and S4 (Supporting Information). This approach has the combined benefit of enhanced absorption at the pump

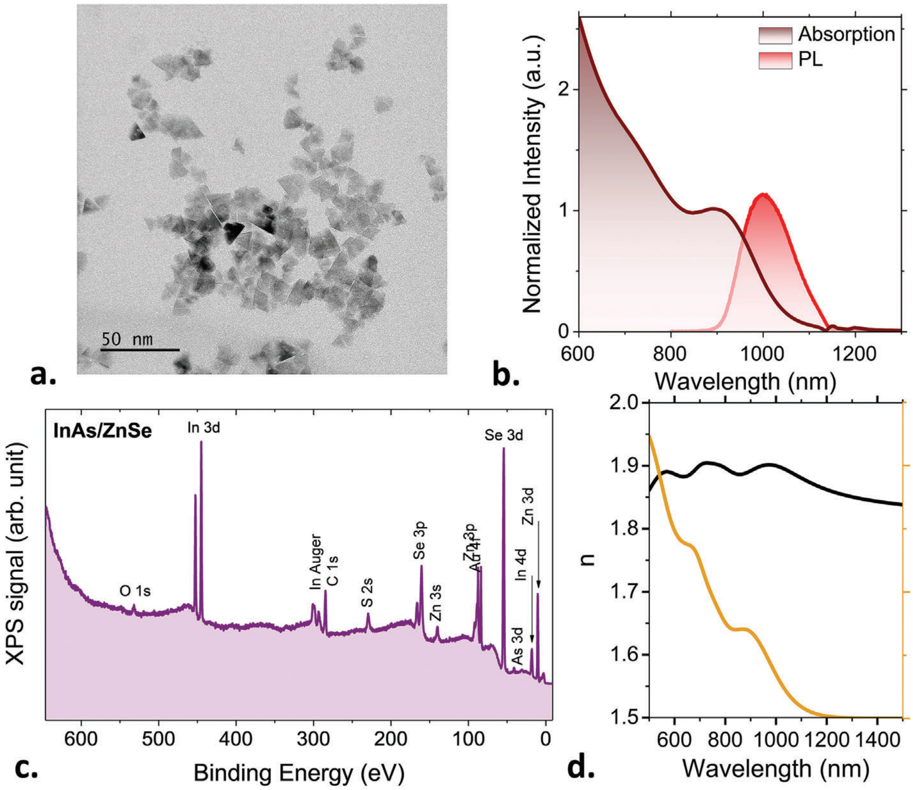

Figure 1. InAs/ZnSe CQD for near-infrared photonics. a) TEM image of the InAs/ZnSe core-shell CQDs. b) Absorption and PL spectra of the CQDs in toluene. c) Photoemission survey spectrum from InAs/ZnSe core-shell CQDs acquired using a photon energy of 700 eV (the core levels analysis is given in Figures S1–S2, Supporting Information). d. Spectrally defined refractive index and extinction coefficient for a thin film of InAs/ZnSe core-shell CQDs with native oleylamine ligands.

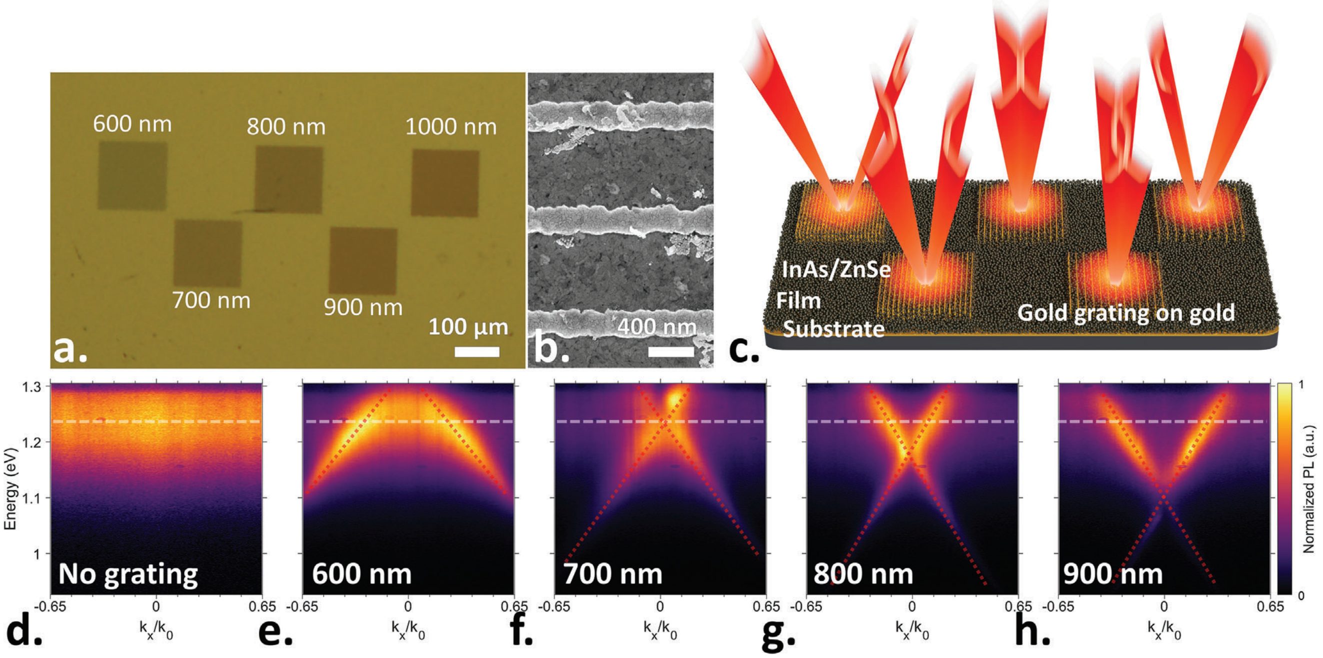

Figure 2. CQD array coupled to plasmonic gratings. a) Optical microscopy image of the grating fabricated on a gold-coated substrate. b) Scanning electron microscopy image of one grating. c) Schematic of a CQD film deposited on the plasmonic gratings with various periods. d) Dispersion map (energy as a function of wavevector) for the CQDs on gold (i.e., away from the grating). e–h) Dispersion map for the CQDs on gratings with increasing periods. The white dashed lines are used as guidelines for the uncoupled PL while red lines guide the contribution from the plasmon.

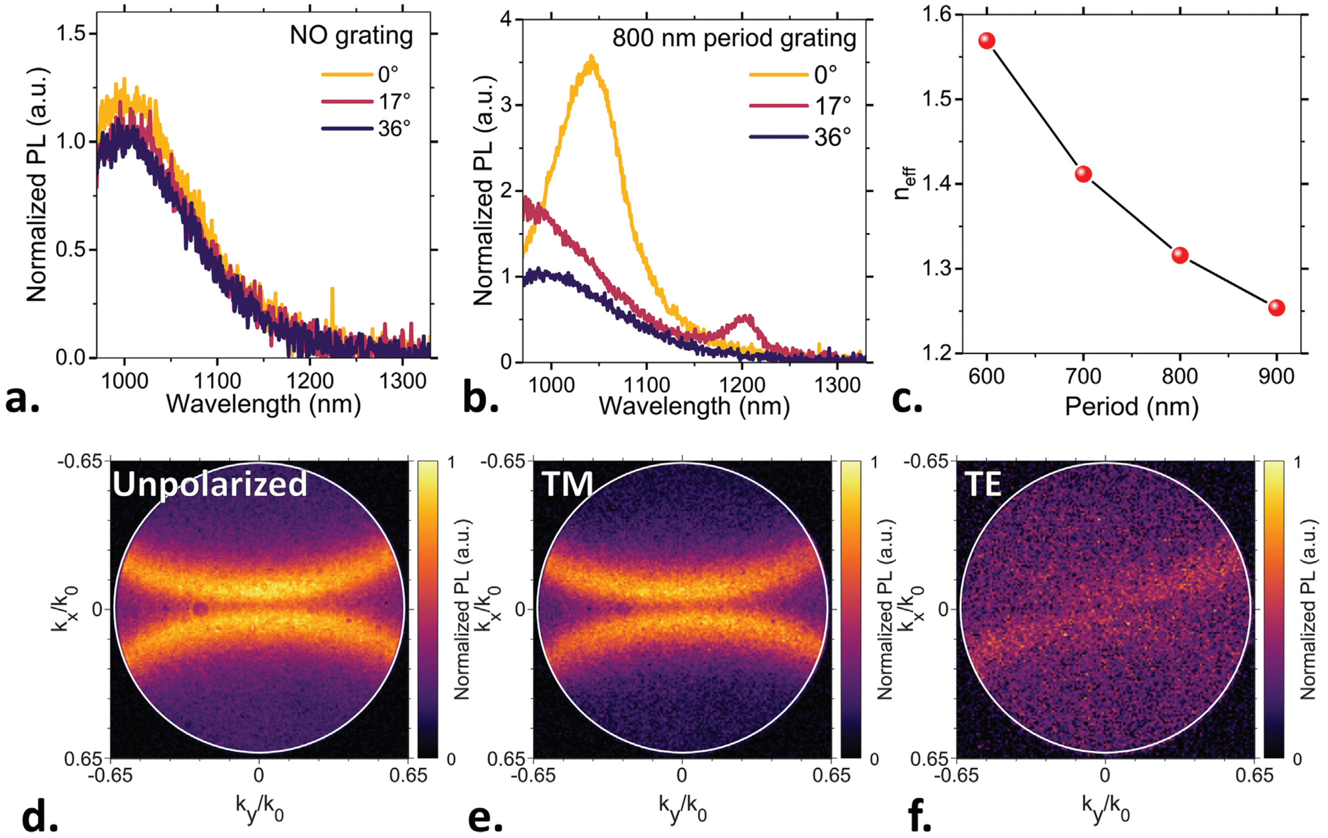

Figure 3. Directivity of the emission. a) PL spectra along three directions for the InAs/ZnSe core-shell CQD film deposited on gold. b) PL spectra along three directions for the InAs/ZnSe core-shell CQD film deposited on an 800 nm period grating. c) Effective index extracted from the dispersion map as a function of the grating period. d) (resp. e.; resp. f.) Radiative diagram at 1050 nm showing the PL intensity as a function of the sine of the emission angle for the unpolarized (resp. TM, resp. TE) PL from InAs/ZnSe CQDs film deposited on the 800 nm period grating. The white circle has a radius of 0.65, corresponding to the NA of the collection objective of our apparatus.

wavelength and a magnified electromagnetic field at the emission wavelength. The resonance wavelength (λ_r) is given by n_{eff}.p with n_{eff} the effective index and p the period of the grating. To obtain a resonance at 1020 nm with a refractive index of 1.9, the expected value of the period should be ≈550 nm. However, the electromagnetic field generated by the plasmon modes is not always located solely within the CQDs layer. The refractive index of the material is thus averaged with the index of the environment, only giving an upper bound for the effective index value. This is why we build a series of gratings with periods ranging from 600 to 1000 nm by steps of 100 nm to be sure to match the grating resonance to the PL maximum of the CQDs, see Figures 2b and S5 (Supporting Information). Due to their small period, we use e-beam lithography for the grating fabrication, see Figure 2c. The functionalized substrate is then coated with the InAs/ZnSe core-shell CQDs without further processing. Thin films are targeted (70–80 nm range), since they ensure a stronger coupling to the plasmon as opposed to the case of thick films where the upper part of the film is less coupled, leading to the superposition of the signal from the uncoupled PL and that related to the plasmon coupling.

The film is then illuminated using a red laser (He-Ne line at 633 nm) and imaged using an optical microscope. The infrared PL is isolated from the visible wavelengths with dichroic mirrors and long-pass filters, then collected through a grating spectrometer and onto an InGaAs camera. We use an objective with a 0.65 numerical aperture, which matches the angular range of emission outcoupled from inside an LED made on glass. The critical angle for total internal reflection is given by $\theta_c = \text{asin}(1/1.5) \approx 40°$, where factor 1.5 accounts for the refractive index of glass. The imaging of the back focal plane enables a direct measurement of the dispersion map (i.e., energy as a function of incident wavevector), see Figure 2d–h. The PL of the pristine core/shell material displays a non-dispersive E-k diagram, as illustrated in Figure 2d. This situation drastically contrasts with the PL signal emitted by the material on top of a grating. There, the PL appears as two dispersive branches crossing each other. These two branches correspond to the dispersion of the orders +1 and −1 of the surface plasmon. The energy at which they cross strongly depends on the grating period, following the equation $n_{eff} = \lambda_{crossing}/p$ where $\lambda_{crossing}$ is the wavelength at which they cross and n_{eff} the effective index of the plasmon. The values of n_{eff} are given in **Figure 3c**. As anticipated from simulations, the values are reduced compared to the refractive index of the nanocrystal film, see Figure 1d. The overall trend is a drop in the effective index with the grating period which reflects the fact that the mode is less and less confined at the metal/CQD interface and leaks more and more in the air. Since SPP modes occur in transverse magnetic (TM) polarization

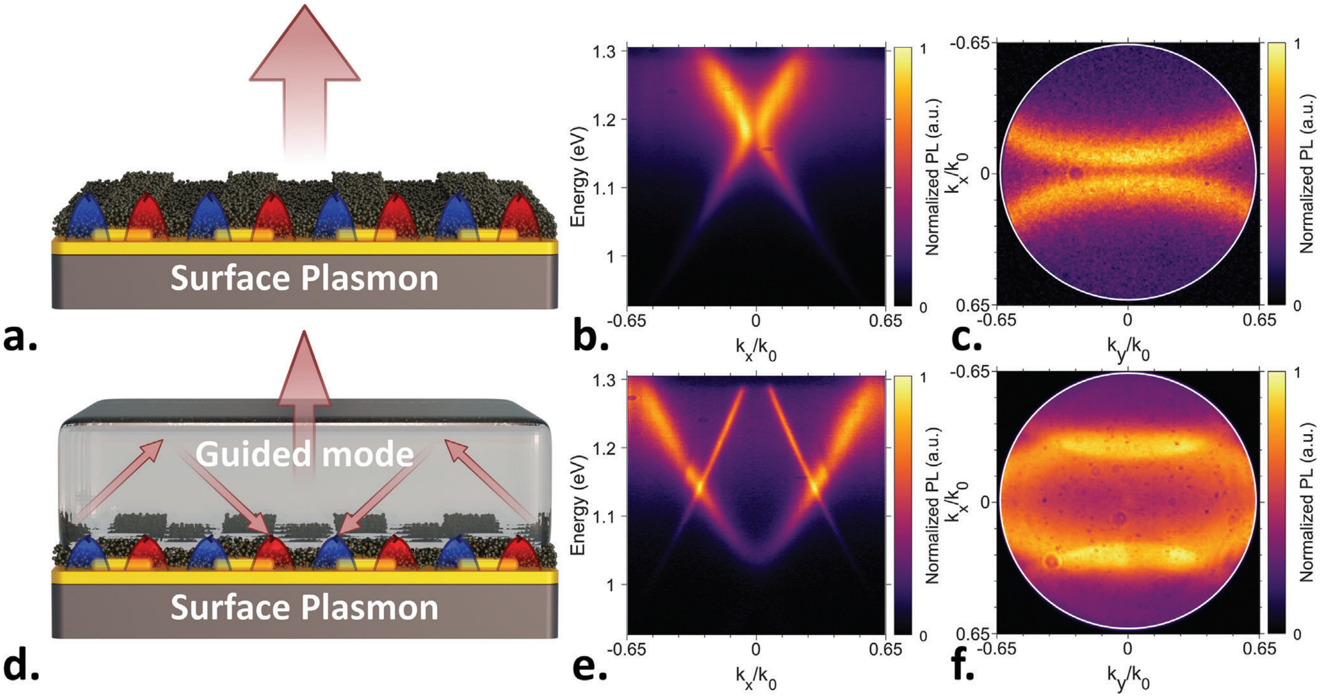

Figure 4. Impact of further integration of the grating. a) (resp. d.) Schematic of the InAs/ZnSe core-shell CQD film deposited on a gold grating fabricated on a gold mirror (resp. with an extra 285 nm of PMMA atop the CQD film). b) (resp. e) Dispersion map for the CQD film on an 800 nm grating period without (resp with) PMMA encapsulation for the unpolarized signal. c) (resp. f.) Radiative diagram for the CQD on an 800 nm grating period without (resp. with) PMMA encapsulation. Polarized signals (TM and TE) are given in Figure S6 (Supporting Information).

only, the PL signal in transverse electric (TE) remains unpolarized, see Figure S5 (Supporting Information) for the measurement and Figure S6 (Supporting Information) for the simulation.

Here, we use the dispersion of the plasmon as a strategy to induce directivity for the emission. In agreement with the dispersion map, the PL of the uncoupled material shows no angular dependence, see Figure 3a. For the material on the grating, a preferential direction appears, which depends on the relative position between the crossing point of the two plasmon branches and the maximum of the uncoupled PL energy. When both are matched as is the case for the 800 nm period, the emission occurs preferentially normal to the substrate, which corresponds to the targeted emission for LEDs, Figure 3b. For this period, an increase by a factor of 3 is observed at normal incidence compared to the off-normal signal. For other periods, the PL matches the plasmon branches at $k \neq 0$, resulting in a favored emission at an oblique angle.

The directive character of the emission is also well illustrated by imaging the back focal plane of the emission that gives access to the radiation pattern, see Figure 3d–f. The TE polarization shows an isotropic emission, while the TM polarization clearly shows emission along a preferential direction. The full width at half maximum of the pattern is determined to be $\approx 15°$.

In the last part of the study, we test the robustness of this approach for later integration into an LED. For this purpose, it is critical for the generated mode not to be too strongly affected by the modification of the CQDs electromagnetic environment. Here, we use a model system that is a polymethyl methacrylate (PMMA) layer, acting as both an encapsulant to prevent possible oxidation of the material and as a model for an LED stack. We additionally design the thickness of the PMMA layer (280–300 nm) to generate an additional guided mode, as discussed in the following.

Figure 4 compares the PL of the film deposited on a grating with (bottom part – Figure 4d–f) and without (top part-Figure 4a–c) a PMMA layer. The dispersion maps display two main changes. First, the crossing energy for the two branches of the plasmon is shifted by the addition of PMMA, thus affecting the preferential direction of the emission. This can be attributed to an increase in the effective index of the plasmon, coming from the increased index of PMMA compared to air. However, the plasmon is still active and the shift can be balanced by reducing the period. Second, we see a second pair of dispersive bands appearing. A polarization study (Figure S7, Supporting Information) confirms that the plasmon mode is still present along the TM polarization, while the new feature made of narrower lines actually occurs in TE polarization (Figure 4e). The simulation of the mode shows that the spatial distribution of the latter is mostly located in PMMA, though leaking enough into the CQD layer to enable PL coupling. The sharpness of the line in the dispersion diagram is directly connected to the absorption of the mode. This new mode, being located in PMMA which is mostly transparent in the near IR, presents sharper lines than the plasmon mode which is located at the metal/CQD interface, where both materials absorb. An additional benefit of the PMMA coating is evident by looking at the radiative pattern. For the grating-only structure, only the TM polarization is directive, whereas the TE mode remains isotropic. With the PMMA overcoating, the emergence of the dispersive guided mode gives this polarization additional directivity, see Figure S8 (Supporting Information).

The benefit of this approach can be quantified by looking at the ratio of intensity of the overall PL to the uncoupled PL, for different angles and at the maximum energy of the uncoupled PL. Without PMMA, the plasmon coupling leads to an increase by a factor of 4 compared to the uncoupled PL. This benefit is reduced in the presence of PMMA, reaching a factor of 3; however, this increase is present in both TM and TE polarizations, leading to a better overall outcoupling.

3. Conclusion

To summarize, we propose a strategy to couple III–V near-infrared emitting CQDs to a plasmonic grating to achieve directive emission, an important step toward better outcoupled light-emitting diodes. Our study focuses on the case of core-shell heterostructures that are found to provide stable PL emission with a strongly reduced tendency for oxidation with respect to core-only structures. Dispersion mapping demonstrates that the PL switches from a non-dispersive mode for the pristine material to a plasmon-dominated mode for the same material placed on the metallic grating. Fine control of the emission direction can be obtained by varying the period of the grating. Our method enables a concentration of the emission within a sub-critical angle cone by a factor of at least 3. The encapsulation of the film within a model stack brings the extra benefit of making the TE polarization directive which further increases the total light outcoupling of the PL.

4. Experimental Section

Chemicals: Indium(I) chloride (In(I)Cl, 99.995%) was purchased from Fisher. Tri-*n*-butylphosphine (TBP, 99%, anhydrous), selenium powder (Se, 99.54%, 100 mesh), zinc chloride ($ZnCl_2$, ≥98%), oleylamine (OLA, ≥98% primary amine), chloroform (anhydrous), methyl acetate (anhydrous), acetone (anhydrous), sodium sulfide nonahydrate ($Na_2S.9H_2O$, ≥99.99% trace metals basis) and tetrachloroethylene (>99%, anhydrous) were purchased from Merck. Ethanol absolute (EtOH, >99.8%) and isopropanol (IPA) were purchased from VWR. Tri-n-octylphosphine (TOP, 97%) was purchased from STREM. All chemicals were used without further purification.

Preparation of the Arsenic Precursor: In an Ar-filled glovebox, 75 µL of tris(dimethylamino)arsine (DMAAs) in 1 mL of degassed OLA was heated at 50 °C for 10 min.

Preparation of 1 M TOP-Se Precursor: In an Ar filled glovebox, 7.5 mmol of Se powder was mixed with 7.5 mL of TOP and heated to 50 °C for an hour under constant stirring until full dissolution of selenium.

Preparation of 0.8 M $ZnCl_2$-OLA Precursor: In an Ar filled glovebox, a mixture of 2 mmol $ZnCl_2$ and 2.5 mL of OLA was heated at 50 °C overnight.

InAs Core Synthesis: InAs CQDs synthesis was performed following a slightly modified published procedure:[14] InCl (1.25 mmol, 3.1 eq), 0.75mL TBP, and 18 mL of OLA were loaded into a 50 mL three-neck round-bottom flask equipped with a magnetic stirring bar and reflux condenser. The mixture was then degassed under vacuum at 50 °C for an hour and heated to 210 °C under argon. Once the reaction mixture reached 210 °C, 1 mL of arsenic precursor was rapidly injected into the reaction mixture under vigorous stirring. After one hour, the reaction was stopped by cooling down the flask to room temperature. 0.5 mL of the crude sample was then centrifuged (10 000 rpm, 1 min). The supernatant solution was collected to give a crude colloidal solution of InAs QDs.

ZnSe Shell Synthesis: The ZnSe shell was synthesized following a published procedure.[31] 3 mL of InAs crude solution was transferred in the three-neck round-bottom flask equipped with a magnetic stirring bar and reflux condenser under argon. The solution was then heated to 80 °C, subsequently, 7.5 mL of TOP-Se and 2.5 mL of $ZnCl_2$-OLA were injected. The reaction mixture was then heated to 310 °C. The reaction was stopped after 5 h by cooling down the reaction mixture to room temperature.

Purification of InAs/ZnSe CQDs: 0.5 mL of crude colloidal solution was mixed with 0.5 mL of anhydrous chloroform, 3 mL of anhydrous methyl acetate, and 3 mL of anhydrous acetone. The resulting suspension was centrifuged (8000 rpm, 2 min). The precipitate was dispersed in 0.5 mL of anhydrous TCE for further characterization.

Transmission Electron Microscopy: A drop of a diluted CQDs solution was drop-casted on a copper grid covered with an amorphous carbon film. The grid was degassed overnight under a secondary vacuum. Imaging was conducted using a JEOL 2010 transmission electron microscope operated at 200 kV.

X-Ray Photoemission Measurements (XPS): For photoemission spectroscopy, the Tempo beamline of synchrotron Soleil was used. Samples were handled in the glove box. A ligand exchange solution was prepared by dissolving $Na_2S.9H_2O$ in ethanol (10 mg mL^{-1}). The solution of InAs/ZnSe CQDs was diluted nine times in toluene, then drop-cast onto a gold-coated SiO_2/Si substrate. In total, two layers were drop-cast. For each layer, the sample was dipped in the ligand exchange solution for 30 s and then rinsed in ethanol for 10 s. The sample was kept under a nitrogen atmosphere before its introduction in the ultra-high vacuum photoemission setup. Samples were introduced in the preparation chamber and degassed until a vacuum below 10^{-9} mbar was reached. Then samples were introduced into the analysis chamber. The signal was acquired by a MBS A-1 photoelectron analyzer. The acquisitions were done at constant pass energy (50 eV) within the detector. Photon energy of 150 eV was used for the acquisition of the valence band while 700 eV photon energy was used for the analysis of the core levels. The zero binding energy (BE) reference (i.e., the Fermi level) was taken at the leading edge of a clean Au film. The acquired data were processed by subtracting a Shirley/linear background and using Voigt curves for peak fitting.

Spectroscopic Ellipsometry: Ellipsometry measures the changes in the polarization state between the incident and the reflected light characterized by the angles ψ and Δ.

$$\rho = \frac{r_p}{r_s} = \left|\frac{r_p}{r_s}\right| e^{i\left(\delta_p - \delta_s\right)} = \tan\psi \; e^{i\Delta} \tag{1}$$

where r_p and r_s are the reflection coefficients of p and s polarized light respectively and where δ_p.and δ_s are the phase shifts at reflection in p and s polarizations, respectively. The measurements were performed on a V-VASE ellipsometer (J.A. Woollam) in the 500–1500 nm range in steps of 5 nm and at 3 angles of incidence of 50, 60, and 70°. The optical constants of the films were described as a superposition of Tauc-Lorentz and Gauss oscillators and inserted in an effective medium approximation to account for the air and ligands in the films.

Simulations: The optical properties of the structure were simulated using the finite element method (FEM) software COMSOL Multiphysics, *2D Frequency Domain Interface*. A Floquet periodicity was set as the boundary conditions for the edges on the left and right of the model. An exciting periodic port was placed above the structure, separated by 20 µm of air to avoid nonphysical interferences. The top-most region was defined as a perfectly matched layer to absorb outgoing waves and minimize possible nonphysical reflections due to the limited model size.

The total thickness of air was chosen to be 30 µm to avoid nonphysical interferences. The thickness of the gold stripes was set to 50 nm. The thickness of the alumina layer was set to 40 nm. To account for uncertainty acquired during fabrication, the thicknesses of the InAs/ZnSe and PMMA layers as well as the width of the stripes were left as adjustable parameters within a reasonable range (70-90 nm for InAs/ZnSe, 200–250 nm for PMMA, and 350–450 nm for the stripe width). These parameters were then set on a case-by-case basis to best match the experimental results.

The relevant optical property of the materials, the complex optical index, was obtained: from COMSOL's built-in database for alumina, air, and PMMA; from a Drude model for gold: $\varepsilon(E) = 1–2.29 \times 10^7 / [E(E+i130)]$, with E the photon energy in meV; from optical ellipsometry for the NC layer.

A physics-controlled mesh was enabled with extremely fine element size.

The reflectance of the structure was determined by integrating the absolute value of the time-averaged power outflow over a boundary placed behind the "on" port and dividing it by the input power defined in the port. The dissipated power per unit volume in the metals and CQDs can be calculated using the formula $P = -0.5\omega |F|^2 Im(\varepsilon)$, where F is the electric field, ω is the angular frequency of the incident wave, and $Im(\varepsilon)$ is the imaginary part of the material permittivity. The absorption of one material was calculated by integrating the dissipated power over the volume of the material, and then by dividing by the incident power defined in the port. Finally, the angular dispersion of the photoluminescence can be simulated using the reciprocity principle between near-field excitation and far-field emission:[46] the far-field emission from the structure with integrated incoherent emitters was reciprocal to the intensity of the near-field excited in the structure by the incident external light averaged over the position of the emitters. Thus:

$$P(\theta, \phi; \lambda) \propto P_i(\lambda) \times \iiint_V |E(\theta, \phi; \lambda; r)|^2 \, d^3 r \tag{2}$$

where $P(\theta,\phi;\lambda)$ is the power emitted from the structure in the direction (θ,ϕ), at wavelength λ, $P_i(\lambda)$ is the power emitted at wavelength λ by a single emitter (obtained from the measurement of the PL of CQDs in solution), V is the volume of CQDs, and $E(\theta,\phi; \lambda; r)$ the local electric field in position r excited by a plane wave of wavelength λ, and incident along the direction (θ,ϕ) (obtained from solving Maxwell's equations using COMSOL).

Grating Fabrication: In a cleanroom, 5 nm of Ti and 80 nm of Au were deposited on Si/SiO_2 substrates (400 nm oxide layer) by thermal evaporation. After deposition, the substrates were thoroughly washed by first spraying them with acetone and then sonicating them in an acetone bath for 5 min. Acetone was sprayed a second time followed by IPA, which was dried with N_2. The substrates were then put into an O_2 plasma cleaner for 7 min at 30 W. Once the substrates were cleaned, PMMA was deposited on top to prepare them for E-beam lithography. Roughly 300 nm of PMMA were deposited by spin-coating a pre-prepared solution of PMMA in anisole at 4000 rpm for 30 s, followed by 3 min of annealing at 175 °C on a heating plate. Thus prepared, the substrates were put into a Zeiss Supra 40 SEM with Raith ELPHYS Quantum device, and e-beam lithography was performed according to the grating design. The operating bias was set to 20 kV, and the aperture to 10 µm. The dose was set depending on the grating period (600 nm and 700 nm: 140 µC cm^{-2}; 800 nm: 145 µC cm^{-2}; 900 and 1000 nm: 150 µC cm^{-2}). The PMMA was then developed in an MIBK:IPA solution (1:3) for 60 s, then washed with IPA and dried with N_2. The developed substrates were cleaned in an O_2 plasma cleaner for 3 min at 30 W. Using a VINCI thermal evaporator, 50 nm of Au were deposited. The PMMA was lifted-off by putting the substrates in acetone for 1 day. Once cleaned a last time for 3 min in an O_2 plasma cleaner at 30 W, the substrates were ready for film deposition.

Alumina Layer Deposition: When needed, an alumina spacer was introduced between the gold grating and the CQD film. An Anric AT-400 Atomic Layer Deposition (ALD) system was employed to deposit 40 nm of Al_2O_3. 450 cycles of ALD were performed, each with pulsed trimethylaluminium (TMA) and H_2O reacted at 175 ^{0}C. The Al_2O_3 film thickness was measured with reflectometry after the deposition.

Thin Film Deposition: InAs/ZnSe CQDs were deposited on the clean substrates into a thin film by spin-coating at 3000 rpm for 60 s. The concentration of the CQD solution was tuned until the thickness of the film deposited on a glass substrate reached 100 nm. The same concentration and spin-coating parameters were then used for all substrates. When needed, a subsequent layer of PMMA was deposited by spin-coating a 25 g L^{-1} solution of PMMA in acetone at 2000 rpm for 45 s directly on top of the CQDs. The depositions were performed in a glovebox to prevent oxidation.

Photoluminescence Characterization of the Grating: The photoluminescence was measured using an Olympus BX51WI upright microscope that focuses the light emitted by a HeNe laser (wavelength 633 nm) onto the surface of the samples. The 50X near-infrared objective used for this optical pumping also serves to collect the photoluminescence. The latter was separated from the optical pump with a Thorlabs DMLP950R dichroic mirror and imaged onto an InGaAs camera (Princeton Instruments NIRvana 640ST) with the help of a 20 mm Telan lens (an additional longpass colored glass filter was put in front of the camera to remove any remnant of visible light). To obtain a dispersion map (i.e. mapping in the k space), a 30 mm Bertrand lens was inserted in the optical path after the dichroic mirror to image the back focal plane of the microscope objective. A monochromator (Princeton Instruments Acton SP2356) mounted before the InGaAs camera provides the spectral information.

Supporting Information

Supporting Information is available from the Wiley Online Library or from the author.

Acknowledgements

The project was supported by ERC grants, FORWARD (grant no 771688), and AQDtive (grant no101086358). The authors acknowledge the use of clean-room facilities from the "Centrale de Proximité Paris-Centre". This work was supported by French state funds managed by the Agence Nationale de la Recherche through the grant Bright (ANR-21-CE24-0012), MixDFerro (ANR-21-CE09-0029), Quicktera (ANR-22-CE09-0018), camIR (ANR-24-CE42), Dirac, Piquant (ANR-24-CE09).

Conflict of Interest

The authors declare no conflict of interest.

Data Availability Statement

The data that support the findings of this study are available from the corresponding author upon reasonable request.

Keywords

III–V quantum dots, plasmon, photoluminescence, infrared

Received: June 14, 2024
Revised: September 9, 2024

---

[1] B. T. Diroll, B. Guzelturk, H. Po, C. Dabard, N. Fu, L. Makke, E. Lhuillier, S. Ithurria, *Chem. Rev.* **2023**, *123*, 3543.
[2] M. A. Hines, P. Guyot-Sionnest, *J. Phys. Chem.* **1996**, *100*, 468.
[3] X. Liang, E. G. Durmusoglu, M. Lunina, P. L. Hernandez-Martinez, V. Valuckas, F. Yan, Y. Lekina, V. K. Sharma, T. Yin, S. T. Ha, Z. X. Shen, H. Sun, A. Kuznetsov, H. V. Demir, *ACS Nano* **2023**, *17*, 19981.
[4] Y. S. Park, J. Lim, N. S. Makarov, V. I. Klimov, *Nano Lett.* **2017**, *17*, 5607.
[5] O. I. Micic, C. J. Curtis, K. M. Jones, J. R. Sprague, A. J. Nozik, *J. Phys. Chem.* **1994**, *98*, 4966.

[6] D. Franke, D. K. Harris, L. Xie, K. F. Jensen, M. G. Bawendi, *Angew. Chem.- Int. Ed.* **2015**, *54*, 14299.
[7] Y. W. Cao, U. Banin, *J. Am. Chem. Soc.* **2000**, *122*, 9692.
[8] V. Grigel, D. Dupont, K. De Nolf, Z. Hens, M. D. Tessier, *J. Am. Chem. Soc.* **2016**, *138*, 13485.
[9] M. Yarema, M. V. Kovalenko, *Chem. Mater.* **2013**, *25*, 1788.
[10] S. Tamang, K. Kim, H. Choi, Y. Kim, S. Jeong, *Dalton Trans.* **2015**, *44*, 16923.
[11] W. Liu, A. Y. Chang, R. D. Schaller, D. V. Talapin, *J. Am. Chem. Soc.* **2012**, *134*, 20258.
[12] T. Sheikh, W. J. Mir, S. Nematulloev, P. Maity, K. E. Yorov, M. N. Hedhili, A. H. Emwas, M. S. Khan, M. Abulikemu, O. F. Mohammed, O. M. Bakr, *ACS Nano* **2023**, *17*, 23094.
[13] R. Yadav, Y. Kwon, C. Rivaux, C. Saint-Pierre, W. L. Ling, P. Reiss, *J. Am. Chem. Soc.* **2023**, *145*, 5970.
[14] M. Ginterseder, D. Franke, C. F. Perkinson, L. Wang, E. C. Hansen, M. G. Bawendi, *J. Am. Chem. Soc.* **2020**, *142*, 4088.
[15] J. C. Ondry, A. Gupta, Z. Zhou, J. H. Chang, D. V. Talapin, *ACS Nano* **2024**, *18*, 858.
[16] A. Gupta, J. C. Ondry, M. Chen, M. H. Hudson, I. Coropceanu, N. A. Sarma, D. V. Talapin, *Nano Lett.* **2022**, *22*, 6545.
[17] L. Asor, J. Liu, Y. Ossia, D. C. Tripathi, N. Tessler, A. I. Frenkel, U. Banin, *Adv. Funct. Mater.* **2021**, *31*, 2007456.
[18] L. Asor, J. Liu, S. Xiang, N. Tessler, A. I. Frenkel, U. Banin, *Adv. Mater.* **2023**, *35*, 2208332.
[19] D. Mocatta, G. Cohen, J. Schattner, O. Millo, E. Rabani, U. Banin, *Science* **2011**, *332*, 77.
[20] W. J. Mir, T. Sheikh, S. Nematulloev, P. Maity, K. E. Yorov, A. H. Emwas, M. N. Hedhili, M. S. Khan, M. Abulikemu, O. F. Mohammed, O. M. Bakr, *Small* **2023**, *20*, 2306535.
[21] A. Gupta, J. C. Ondry, K. Lin, Y. Chen, M. H. Hudson, M. Chen, R. D. Schaller, A. J. Rossini, E. Rabani, D. V. Talapin, *J. Am. Chem. Soc.* **2023**, *145*, 16429.
[22] A. Saha, R. Yadav, D. Aldakov, P. Reiss, *Angew. Chem., Int. Ed.* **2023**, *62*, 202311317.
[23] L. Peng, Y. Wang, Y. Ren, Z. Wang, P. Cao, G. Konstantatos, *ACS Nano* **2024**, *18*, 5113.
[24] Muhammad, D. C, D. H. Parmar, B. Rehl, Y. Zhang, O. Atan, G. Kim, P. Xia, J. M. Pina, M. Li, Y. Liu, O. Voznyy, S. Hoogland, E. H. Sargent, *Adv. Mater.* **2023**, *35*, 2306147.
[25] P. Xia, B. Sun, M. Biondi, J. Xu, O. Atan, M. Imran, Y. Hassan, Y. Liu, J. M. Pina, A. M. Najarian, L. Grater, K. Bertens, L. K. Sagar, H. Anwar, M. J. Choi, Y. Zhang, M. Hasham, F. P. García de Arquer, S. Hoogland, M. W. B. Wilson, E. H. Sargent, *Adv. Mater.* **2023**, *35*, 2301842.
[26] M. Vafaie, A. M. Najarian, J. Xu, L. J. Richter, R. Li, Y. Zhang, M. Imran, P. Xia, H. W. Ban, L. Levina, A. Singh, J. Meitzner, A. G. Pattantyus-Abraham, F. Pelayo García de Arquer, E. H. Sargent, *Proc. Natl. Acad. Sci. USA* **2023**, *120*, 2305327120.
[27] B. Sun, A. M. Najarian, L. K. Sagar, M. Biondi, M. J. Choi, X. Li, L. Levina, S. W. Baek, C. Zheng, S. Lee, A. R. Kirmani, R. Sabatini, J. Abed, M. Liu, M. Vafaie, P. Li, L. J. Richter, O. Voznyy, M. Chekini, Z. H. Lu, F. P. García de Arquer, E. H. Sargent, *Adv. Mater.* **2022**, *34*, 2203039.
[28] J. Leemans, V. Pejović, E. Georgitzikis, M. Minjauw, A. B. Siddik, Y. H. Deng, Y. Kuang, G. Roelkens, C. Detavernier, I. Lieberman, P. E. Malinowski, D. Cheyns, Z. Hens, *Adv. Sci.* **2022**, *9*, 2200844.
[29] Y. Wang, Z. Liu, N. Huo, F. Li, M. Gu, X. Ling, Y. Zhang, K. Lu, L. Han, H. Fang, A. G. Shulga, Y. Xue, S. Zhou, F. Yang, X. Tang, J. Zheng, M. Antonietta Loi, G. Konstantatos, W. Ma, *Nat. Commun.* **2019**, *10*, 5186.
[30] B. Martinez, J. Ramade, C. Livache, N. Goubet, A. Chu, C. Gréboval, J. Qu, W. L. Watkins, L. Becerra, E. Dandeu, J. L. Fave, C. Méthivier, E. Lacaze, E. Lhuillier, *Adv. Opt. Mater.* **2019**, *7*, 1900348.
[31] D. Zhu, H. Bahmani Jalali, G. Saleh, F. Di Stasio, M. Prato, N. Polykarpou, A. Othonos, S. Christodoulou, Y. P. Ivanov, G. Divitini, I. Infante, L. De Trizio, L. Manna, *Adv. Mater.* **2023**, *35*, 2303621.
[32] D. Zhu, F. Bellato, H. Bahmani Jalali, F. Di Stasio, M. Prato, Y. P. Ivanov, G. Divitini, I. Infante, L. De Trizio, L. Manna, *J. Am. Chem. Soc.* **2022**, *144*, 10515.
[33] M. De Franco, D. Zhu, A. Asaithambi, M. Prato, E. Charalampous, S. Christodoulou, I. Kriegel, L. De Trizio, L. Manna, H. Bahmani Jalali, F. Di Stasio, *ACS Energy Lett.* **2022**, *7*, 3788.
[34] A. Aharoni, T. Mokari, I. Popov, U. Banin, *J. Am. Chem. Soc.* **2006**, *128*, 257.
[35] V. I. Klimov, *Nanocrystal Quantum Dots*, CRC Press, xx **2010**.
[36] A. I. Ekimov, Al. L. Efros, A. A. Onushchenko, *Solid State Commun.* **1985**, *56*, 921.
[37] Y. Kwon, O. Yeromina, M. Cavallo, M. G. Silly, D. Pierucci, E. Lhuillier, D. Aldakov, B. Hyot, P. Reiss, *Adv. Funct. Mater.* **2024**, 2403912.
[38] S. Adachi, *J. Appl. Phys.* **1982**, *53*, 8775.
[39] E. Bailly, J.-P. Hugonin, J.-R. Coudevylle, C. Dabard, S. Ithurria, B. Vest, J.-J. Greffet, *ACS Nano* **2024**, *18*, 4903.
[40] H. Monin, A. Loirette-Pelous, E. De Leo, A. A. Rossinelli, F. Prins, D. J. Norris, E. Bailly, J.-P. Hugonin, B. Vest, J.-J. Greffet, *Opt. Express.* **2023**, *31*, 4851.
[41] N. E. Watkins, J. Guan, B. T. Diroll, K. R. Williams, R. D. Schaller, T. W. Odom, *J. Phys. Chem. C* **2021**, *125*, 19874.
[42] S. Zhang, Y. Liang, Q. Jing, Z. Lu, Y. Lu, T. Xu, *Sci. Rep.* **2017**, *7*, 14695.
[43] D. Schanne, S. Suffit, P. Filloux, E. Lhuillier, A. Degiron, *Appl. Phys. Lett.* **2021**, *119*, 181105.
[44] E. Bossavit, T. H. Dang, P. He, M. Cavallo, A. Khalili, C. Dabard, H. Zhang, D. Gacemi, M. G. Silly, C. Abadie, B. Gallas, D. Pierucci, Y. Todorov, C. Sirtori, B. T. Diroll, A. Degiron, E. Lhuillier, A. Vasanelli, *Adv. Opt. Mater.* **2023**, *11*, 2300863.
[45] C. Dabard, E. Bossavit, T. H. Dang, N. Ledos, M. Cavallo, A. Khalili, H. Zhang, R. Alchaar, G. Patriarche, A. Vasanelli, B. T. Diroll, A. Degiron, E. Lhuillier, S. Ithurria, *J. Phys. Chem. C* **2023**, *127*, 14847.
[46] A. Vaskin, R. Kolkowski, A. F. Koenderink, I. Staude, *Nanophotonics* **2019**, *8*, 1151.